

# Measurement of the structural behaviour of a 3D airless wheel prototype by means of optical non-contact techniques

Antonino Quattrocchi<sup>1</sup>, Damiano Alizzio<sup>1</sup>, Lorenzo Capponi<sup>2</sup>, Tommaso Tocci<sup>3</sup>, Roberto Marsili<sup>3</sup>, Gianluca Rossi<sup>3</sup>, Simone Pasinetti<sup>4</sup>, Paolo Chiariotti<sup>5</sup>, Alessandro Annessi<sup>6</sup>, Paolo Castellini<sup>6</sup>, Milena Martarelli<sup>6</sup>, Fabrizio Freni<sup>1</sup>, Annamaria Di Giacomo<sup>1</sup>, Roberto Montanini<sup>1</sup>

<sup>1</sup> Department of Engineering, University of Messina, Messina, Italy

<sup>2</sup> Aerospace Department, University of Illinois Urbana-Champaign, Urbana, Illinois, USA

<sup>3</sup> Department of Engineering, University of Perugia, Perugia, Italy

<sup>4</sup> Department of Mechanical and Industrial Engineering, University of Brescia, Brescia, Italy

<sup>5</sup> Department of Mechanical Engineering, Politecnico di Milano, Milan, Italy

<sup>6</sup> Department of Industrial Engineering and Mathematical Sciences, Polytechnic University of Marche, Ancona, Italy

## ABSTRACT

Additive Manufacturing (AM) is becoming a widely employed technique also in mass production. In this field, compliances with geometry and mechanical performance standards represent a crucial constrain. Since 3D printed products exhibit a mechanical behaviour that is difficult to predict and investigate due to the complex shape and the inaccuracy in reproducing nominal sizes, optical non-contact techniques are an appropriate candidate to solve these issues. In this paper, 2D digital image correlation and thermoelastic stress analysis are combined to map the stress and the strain performance of an airless wheel prototype. The innovative airless wheel samples are 3D-printed by fused deposition modelling and stereolithography in poly-lactic acid and photopolymer resin, respectively. The static mechanical behaviour for different wheel-ground contact configurations is analysed using the aforementioned non-contact techniques. Moreover, the wheel-ground contact pressure is mapped, and a parametric finite element model is developed. The results presented in the paper demonstrate that several factors have great influence on 3D printed airless wheels: a) the type of material used for manufacturing the specimen, b) the correct transfer of the force line (i.e., the loading system), c) the geometric complexity of the lattice structure of the airless wheel. The work confirms the effectiveness of the proposed non-contact measurement procedures for characterizing complex shaped prototypes manufactured using AM.

**Section:** RESEARCH PAPER

**Keywords:** additive manufacturing; digital image correlation; thermoelastic stress analysis; finite element modelling; contact pressure mapping

**Citation:** Antonino Quattrocchi, Damiano Alizzio, Lorenzo Capponi, Tommaso Tocci, Roberto Marsili, Gianluca Rossi, Simone Pasinetti, Paolo Chiariotti, Alessandro Annessi, Paolo Castellini, Milena Martarelli, Fabrizio Freni, Annamaria Di Giacomo, Roberto Montanini, Measurement of the structural behaviour of a 3D airless wheel prototype by means of optical non-contact techniques, Acta IMEKO, vol. 11, no. 3, article 13, September 2022, identifier: IMEKO-ACTA-11 (2022)-03-13

**Section Editor:** Francesco Lamonaca, University of Calabria, Italy

**Received** March 17, 2022; **In final form** June 23, 2022; **Published** September 2022

**Copyright:** This is an open-access article distributed under the terms of the Creative Commons Attribution 3.0 License, which permits unrestricted use, distribution, and reproduction in any medium, provided the original author and source are credited.

**Funding:** This work was supported by the Ministry of Education, University and Research in Italy (MIUR) under the Research Project of National Interest (PRIN2015) "Experimental techniques for the characterization of the effective performances of trabecular morphology structures realized in additive manufacturing".

**Corresponding author:** Antonino Quattrocchi, e-mail: [antonino.quattrocchi@unime.it](mailto:antonino.quattrocchi@unime.it)

## 1. INTRODUCTION

Additive Manufacturing (AM) or, more commonly, 3D printing is an emerging manufacturing technique, applied in several fields of Industry [1], [2]. It allows to achieve some

important goals such as weight reduction, development of complex shapes and use of a wide variety of materials [3]. Currently, AM is applied to exploit the design flexibility of numerical topology optimization tools and to lead to the creation of innovative samples [4]. Moreover, AM is not only adopted to produce prototypes, but it can target mass production. The latter

purpose implies compliance with many restrictions due to the need to satisfy the production standards [5]. Functional quality is generally associated with the structural response during the application of static and dynamic loads. However, in 3D printed lattice structures, the mechanical response can be significantly different than expected [6]. The causes of this anomaly can be identified in the geometric complexity and in the inaccurate reproduction of the nominal shape by the AM process [7].

Although finite elements numerical analyses have been performed [8], [9], experimental measurement of the actual structural response of lattice components has a relevant interest for AM technology [10], [11]. Indeed, traditional techniques [12] are not suitable for investigating 3D printing lattice parts, for example, due to the complex structures, non-conventional material, and small size. Non-contact methods represent powerful alternatives, providing remarkable results despite the demanding technological requirements [13], [14]. The state-of-the-art on this topic collects only few works, which often do not investigate in depth the mechanical behaviour of the product obtained. Despite numerical finite elements analyses provide a good overview [15], the experimental mechanical characterization has been generally limited to the estimation of conventional stress-strain curves, carried out by static and dynamic compression tests [16], [17]. Other ancillary analyses were performed for the evaluation of the porosity of the material by scanning electron microscopy [18] and for the investigation of the composition of the crystalline structure of the produced materials by means of backscattering electron diffraction [19].

One of the first examples of experimental mechanical characterization by non-contact methods was discussed by Brenne et al. [20]. They mapped the strain behaviour of a lattice, heat-treated titanium alloy specimen, subjected to both uniaxial and bending loads, using 2D digital image correlation (DIC) [21], [22] and electron backscatter diffraction. The results clarified the effect of the heat-treatment and the weaknesses of the structure, but, unfortunately, the quality of the 2D DIC images [23], [24] did not allow to investigate the performance of the individual beam and to carry out some quantitative results. A more detailed inspection was provided by Vanderesse et al. [25]. They investigated the strain behaviour of porous lattice materials with body cubic-centred reinforced, and diamond mesostructures subjected to quasi-static compression up to failure. The strain maps, obtained using DIC, showed the localization of the most strained areas before and after the sample failure, highlighting a diffuse distribution, strongly depending on the analyzed reticular structure. In fact, it was generally noted that some struts exhibited a critical behavior that quickly led to their collapse, while other ones were slightly strained. Allevi et al. [26] performed a feasibility study of the thermoelastic stress analysis (TSA) [27], [28] on a titanium based-alloy space bracket, made by electron beam melting. Their results showed the same load trends that can be identified on larger scales, but also especially small and unexpected peaks in the TSA output and theoretical outcomes calculated by finite elements analysis. Quattrocchi et al. [29] evaluated the mechanical behavior of a lumbar transforaminal interbody fusion cage implant, made by a 3D printing process adopting medical grade titanium. Although these devices have a trabecular structure, useful for bone development, TSA allowed to identify that at the small scale the complex geometry of the specimen determines local differences in the stress distribution with intensification of the loads at the trabecular knots. Finally, Allevi et al. [30], [31] developed experimental protocols based on advanced non-contact

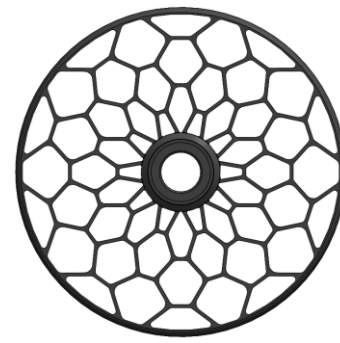


Figure 1. Frontal view of the airless wheel prototype with lattice morphology.

measurement techniques to qualify the full mechanical behaviour of lattice structures. They employed different techniques, such as 2D vision systems, 2D DIC, TSA and laser Doppler vibrometry (LDV), to investigate morphological characteristics, to map local stress-strain fields, and to analyse the modal behaviour of simple lattice structures.

This paper is the extended version of the one presented at the IEEE I2MTC 2020 [32] and focuses on the evaluation of local stress-strain mapping. Consequently, the aim of this work is to measure the mechanical behaviour of an airless wheel [33], [34] with a complex lattice structure, obtained through AM, by adopting non-contact optical techniques. Indeed, unlike traditional methods which are inefficient and even inapplicable in such conditions, non-contact optical techniques are an appropriate candidate for obtaining full-field information without altering the object of the study. Two airless wheel samples, which were manufactured using different printing technologies (fused deposition modelling, FDM, and stereolithography, SLA) and materials (poly-lactic acid, PLA, and photopolymer resin, PPR), have been investigated. A measurement procedure, based on DIC and TSA, has been applied to achieve combined full-field strain and stress measurements of the different wheel-ground contact configurations. Furthermore, the wheel-ground contact pressure (CP) has been mapped estimating the load transfer. Finally, a parametric finite elements model has been developed and compared to the results obtained from the experimental approaches.

## 2. MATERIALS AND METHODS

### 2.1. Airless wheel prototypes

The airless wheel prototype (Figure 1) was specifically manufactured according to [4]. The geometry is designed following a regular pattern of fixed angular amplitude ( $36^\circ$ ). The pattern is then extruded in the axial direction of the same wheel. The lattice structure is obtained by connecting the intersection points of four circular crowns of equal width along the diameter and ten circular sectors of the wheel through a “zig-zag” criterion. The thickness of each trabecula is always kept the same.

While FDM allows to obtain a model by subsequent layering of fused material, SLA adopts a 3D printing method based on a photochemical process. A laser beam is focused on a liquid PPR to enable the wiring and solidification processes of the monomers on a building platform. The raw structure is washed in isopropyl alcohol; the supports useful for the realization of the product are removed and the grafting points of the same supports are smoothed. Finally, a post-cure process is performed to complete the solidification process and to improve the

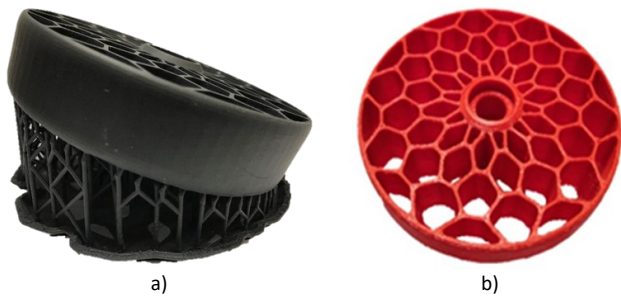


Figure 2. 3D printed samples manufactured by means of: a) SLA and b) FDM technologies.

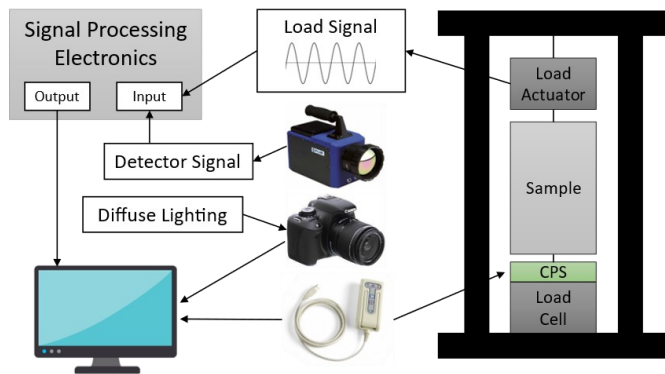


Figure 3. Schematic representation of the experimental setup used for DIC and TSA measurements; CPS = contact pressure sensor.

mechanical properties of the printed structure. The SLA sample (Figure 2 a) was realized by a Form 2 printer (Formlabs Inc., USA) with a standard PPR, while the post-cure process was performed by exposing the raw sample to UV light (wavelength of 405 nm) for 30 min at 60 °C (15 min for each side). Instead, the FDM sample (Figure 2 b) was obtained by Ultimaker 2+ printer (Ultimaker B.V., Utrecht; NL) with PLA. In this case, the post-cure is not necessary. Table 1 reports the parameters adopted for the 3D printing processes.

## 2.2. Experimental setup

The mechanical behaviour was studied using an experimental setup consisting of a loading system, a digital camera with lighting projectors for DIC measurements, an infrared (IR) camera suited to TSA measurements and an acquisition system with a piezoresistive sensor for wheel-ground CP estimation (Figure 3). A rubber tread was not considered yet for the tests performed and discussed in this paper.

The stress and the strain fields were mapped employing specific load stages on the wheel. 2D DIC was performed applying a static load, while TSA was implemented by a dynamic load with harmonic trend. The load was transferred to the wheel by a dedicated apparatus (Figure 4), i.e., a shaft and a loading

Table 1. 3D printing parameters used for the airless wheel prototypes.

AM technique	SLA	FDM
Material	Black V4	PLA Red
Support points size in mm	0.6	-
Layer thickness in $\mu\text{m}$	50	100
Printing time in h	9.15	23.33
Number of layers	1003	258
Material volume or weight	72 ml	56 g
Orientation in $^\circ$	15	0

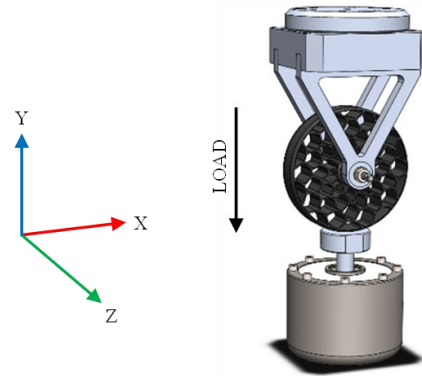


Figure 4. Loading apparatus for DIC and TSA measurements.

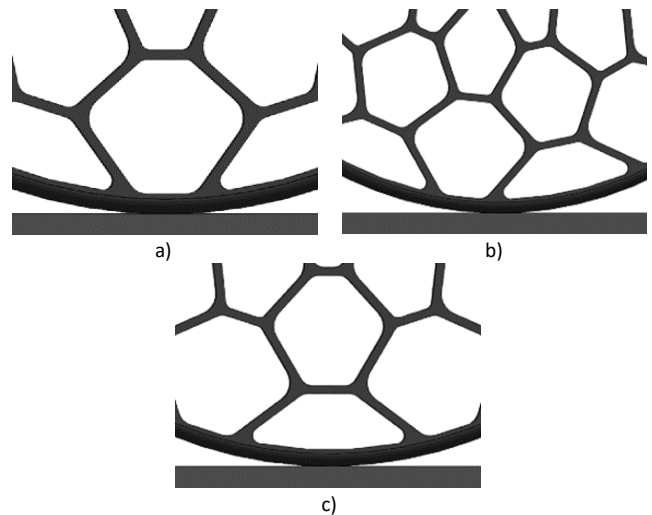


Figure 5. Frontal view of the wheel lattice structure for different wheel-ground contact configurations: a) rhombic, b) mixed and c) trapezoidal.

frame specifically designed and manufactured. The airless wheel was locked by a bolted connection. This arrangement prevented the rotation of the wheel around its axis. The load was then applied in the vertical direction (Y-axis). The loading condition was driven by an actuator and the effective load provided was measured through a load cell. More in detail, two slightly different loading systems were used: an electromechanical material testing machine (mod. ElectroPlus E3000, Instron Company, Norwood, MA, USA) equipped with a calibrated 5 kN load cell was employing during the tests on the SLA wheel, while an electrodynamic shaker (mod. LDS V650, Brüel & Kjær, Nærum, Denmark) with a dedicate power amplification unit was used for the tests on the FDM wheel.

The morphology of the lattice structure of the airless wheel does not guarantee the same the wheel hub stress and strain distributions because these depend on the topology occurring on the angular portion of the wheel corresponding to the wheel contact patch. Consequently, three different contact configurations have been analyzed: mixed, rhombic and trapezoidal; this labelling refers to the frontal geometric topology of the lattice region. (Figure 5).

2D DIC measurements required a preliminary preparation of the target surface (frontal view) of the wheel in order to create a suitable random speckle pattern [35]. This was done by spraying a matt white paint, hence obtaining a high contrast surface given the natural black colour of the wheel material. The images were taken using a Nikkor AF Micro 200 mm lens mounted on a

Table 2. Details of the systems configuration used for 2D DIC measurements.

AM technique	SLA	FDM
Camera	Nikon D3100	Canon EOS 7D
Focus distance in mm	610	550
F-Stop	f/7.1	f/4.5
Exposition time in s	1/40	1/30
ISO* sensitivity	2000	6400
Focal distance in mm	200	100
Images resolution in pixel × pixel	4608 × 3072	1920 × 1080
Loads in N	0 to 200	0 to 250

\* International Organization for Standardization (ISO)

Table 3. Details of the measurement systems.

CP technique	SLA
Software	I-Scan
5040N sensing area (L × W × D) in mm	44.0 × 44.0 × 0.1
5040N sensing resolution in sensel/cm <sup>2</sup>	100.0
Image scale (8 bit) in DL	0-255
Images resolution in pixel × pixel	430×430
Loads in N	0 to 200

Table 4. Details of the systems configuration used for TSA measurements.

AM technique	SLA	FDM
Thermal camera	Flir Titanium SC7200	Flir A6751sc
Software	Altair LI	Flir Research IR + Matlab
Images resolution		
In pixel × pixel	640 × 512	640 × 512
Filter	Low-pass	Median
Load frequency in Hz	5 - 10 - 15	5 - 10 - 15
Preload in N	20 - 50 - 80	50 - 75 - 100
Peak-peak load in N	5 - 10 - 15	20 - 40 - 60

Nikon D3100 digital camera (for the tests on the SLA-printed wheel) and a Canon EF 200m lens with Canon EOS 7D digital camera (for the tests on the FDM-printed wheel). The two imaging systems approximately ensure the same field of view (FOV) but with a different spatial resolution. A diffuse illumination was obtained by exploiting LED light. This was adopted to improve image quality and further increase contrast. Particular attention was paid to checking the image quality and to verifying that no saturation phenomena occurred in the image. DIC tests were carried out at different load levels synchronizing the frame rate to the load increase (i.e., 1 frame recorded every 1 N load increase step). The post-processing of DIC tests was performed off-line, using the GOM Correlate Pro software (GOM GmbH, Braunschweig, Germany). Table 2 reports the details of the two image systems and the load configuration for the 2D DIC measurement.

The wheel-ground CP was acquired during the DIC tests using a flexible, thin and piezoresistive sensor (mod. 5040N), wired to a specific acquisition system (Evolution™ Handle, Tekscan, South Boston, MA, USA) and opting for a sampling frequency of 1 Hz. The characteristics of the CP system are described in Table 3.

TSA was carried out by working in lock-in mode, i.e. by synchronizing IR system frame rate to the harmonic load applied. A preliminary study was conducted to determine the correct excitation parameters. This made it possible to obtain quasi-

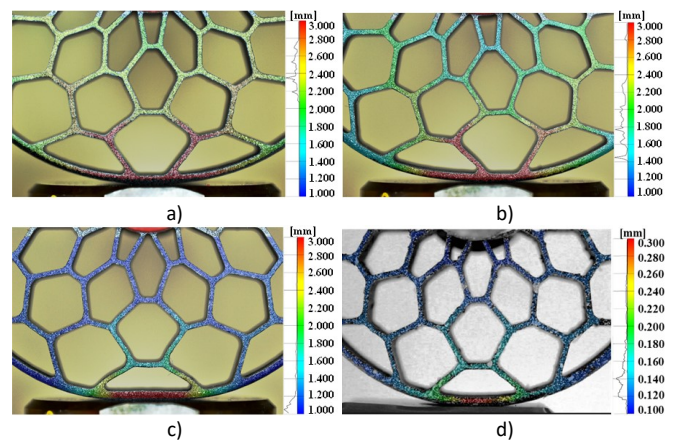


Figure 6. Displacement along the vertical direction (Y-axis) for the airless wheel in different contact configurations: a) rhombic, b) mixed and c) trapezoidal for the PPR sample at 200 N and d) trapezoidal for the PLA one at 250 N; specifically, c) and d) have two distinct scales, different by an order of magnitude.

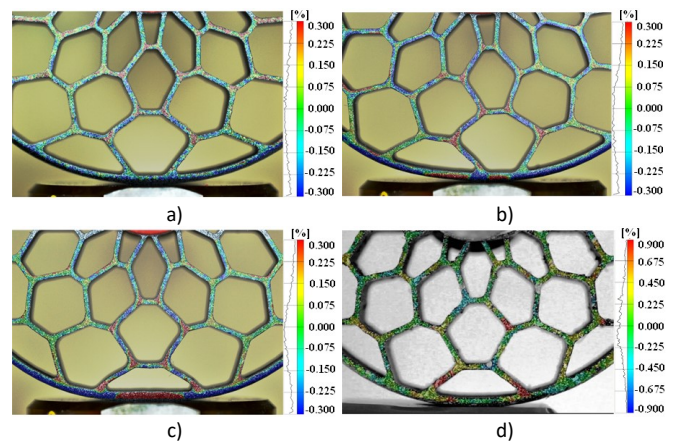


Figure 7. Strain along the vertical direction (Y-axis) for the airless wheel in different contact configurations: a) rhombic, b) mixed and c) trapezoidal for the PPR sample at 200 N and d) trapezoidal for the PLA one at 250 N; specifically, c) and d) have two distinct scales, different by a factor three.

adiabatic conditions and a high signal to noise ratio (SNR) thermoelastic signal. These parameters are highly related to the thermal and mechanical properties of the printing material, more specifically to the heat capacity and stiffness. Consequently, the working parameters are slightly different for the SLA and the FDM prototypes. Tests were performed with specific pre-load and overload levels but employing the same sampling frequency of 100 Hz. The IR images were taken using a FLIR A6751SC camera (SLA-printed wheel) and a FLIR SC7600 one (FDM-printed wheel). Both IR cameras have a spatial resolution of 640 × 512 pixel and an InSb detector with a thermal resolution of 20 mK at the room temperature. Table 4 summarizes the characteristics of the two imaging systems and the load configuration used for the TSA measurements.

### 3. RESULTS AND DISCUSSION

#### 3.1. 2D DIC measurements

As an example, Figure 6 displays the full-field maps of the displacements for the airless wheels along the vertical direction (Y-axis). For the PPR sample (SLA-printed), the displacement is uniformly high on the beams and nodes of the angular portion of the wheel when the wheel-ground contact takes place in the

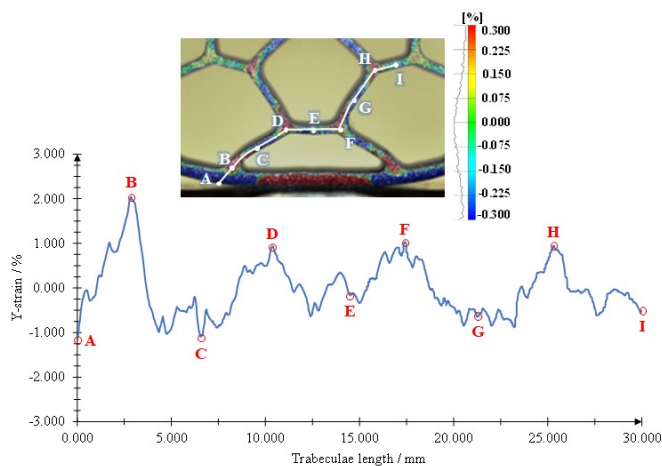


Figure 8. Y-strain along the trabeculae (“white line” in strain map) for the PPR sample in trapezoidal configuration at 200 N.

rhombic and mixed configurations (Figure 6 a and Figure 6 b). The trapezoidal configuration (Figure 6 c) shows a displacement mainly concentrated on the external ring of the wheel rather than on the beams (i.e., the weakest region), considering the unloaded stage. Furthermore, for the rhombic and trapezoidal configurations (Figure 6 a and Figure 6 c), the displacements appear to be symmetrical if comparing the loading line with the other sectors that seem to be relatively unloaded. Finally, by taking into account the trapezoidal configurations of the two types of samples (Figure 6 c and Figure 6 d), they exhibit the same trend, even if the trend of the PLA one (FDM-printed) has a significant reduction. Indeed, even though the PLA sample was subjected to a greater load (25 % more with respect to the PPR sample) the maximum displacement is an order of magnitude less than that of the PPR wheel.

Figure 7 reports the full-field maps of the measured strain for the airless wheels along the vertical direction (Y-axis). In each contact configuration investigated, the strain is well distributed on the lattice structure but concentrated in the nodes. The strain analysis demonstrates that flexural effects prevail, with maximum positive values (i.e. tensile strain) at the vertexes of the beams and maximum negative values (i.e. compressive strain) along the interconnecting segments. A marked symmetry can be highlighted on the trapezoidal and rhombic configurations (Figure 7 a and Figure 7 c). Only for the trapezoidal configuration, the most stressed region corresponds to the sector along the loading line. Specifically, for the PPR sample (Figure 7 c), the external ring of the wheel shows a high strain value on the contact area. Indeed, it is also very clear the elastic behavior of the connecting beams of the lattice structure produced by relatively high loads. Contrarily, although the trend is similar to the one measured in the former case, the PLA sample (Figure 7 d) shows a maximum strain greater than the one of the PPR sample. This could be a consequence of the specific material used for manufacturing and loading the wheel. Indeed, the shaker seemed to be more inefficient in transferring the load with respect to the electromechanical material testing machine, which appeared to be more rigid. The lower level of the effective load transferred to the wheel is reflected in a higher level of noise, which sometimes prevented an accurate identification of the strains.

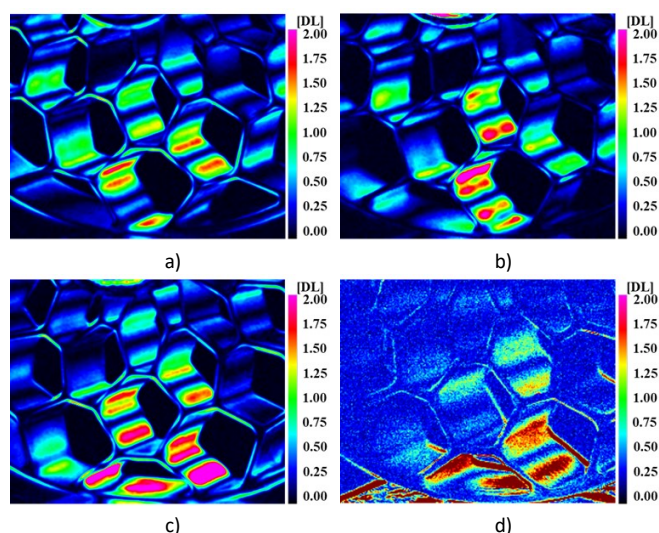


Figure 9. Amplitude of the TSA signal for the airless wheel in different contact configurations: a) rhombic, b) mixed and c) trapezoidal for the PPR samples and d) trapezoidal for the PLA ones (harmonic excitation at 5 Hz, with 15 N peak-to-peak load and 80 N preload).

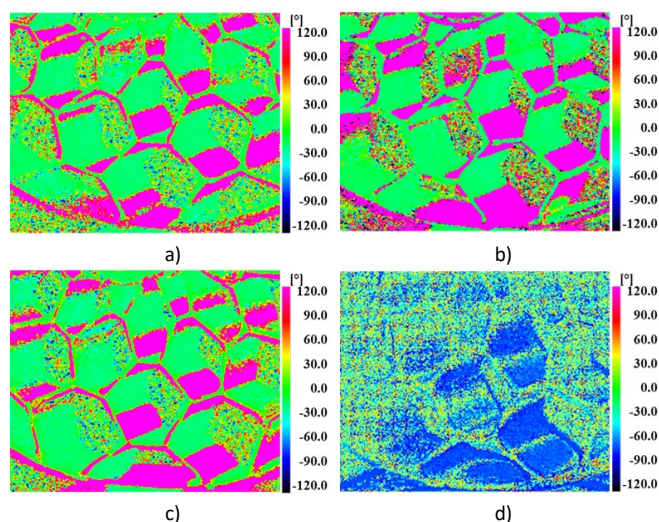


Figure 10. Phase of the TSA signal for the airless wheel in different contact configurations: a) rhombic, b) mixed and c) trapezoidal for the PPR samples and d) trapezoidal for the PLA ones (harmonic excitation at 5 Hz, with 15 N peak-to-peak load and 80 N preload).

Figure 8 exhibits the trend of Y-strain along the trabeculae, from the external ring to the wheel hub, in the trapezoidal configuration for the PPR sample.

As already discussed for Figure 7, Figure 8 highlights the flexural effects on the trabeculae. Indeed, the maximum positive values correspond to the intersections of the trabeculae (points B, D, F and H), while the maximum negative values (close to points C, E, G and I) to the centreline of the individual trabeculae. Furthermore, the considered trabeculae, two for the trapezoidal sector (B-D and D-F) and two for the rhombic sector (F-H and H-I), present approximately a similar trend. This can be sufficiently considered the same for all trabeculae of the wheel.

### 3.2. TSA measurements

In TSA measurements, the lock-in process allows the entire sequence of the recorded IR images to be condensed into only two images that represent the amplitude (Figure 9) and the phase

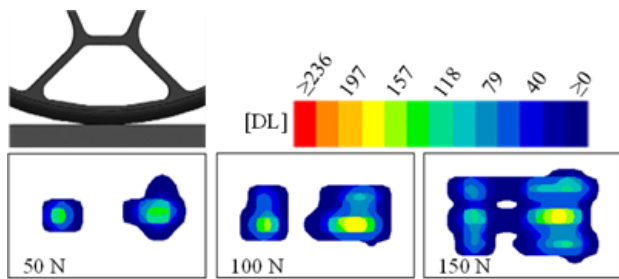


Figure 11. CP map of the trapezoidal configuration for the PPR wheel.

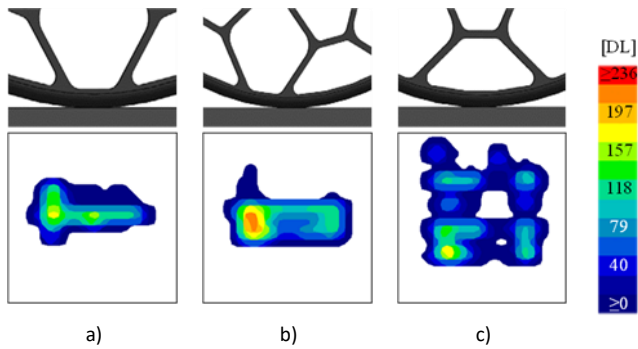


Figure 12. Comparison between the CP maps for the configurations: a) rhombic, b) mixed and c) trapezoidal of the PPR wheel at 200 N.

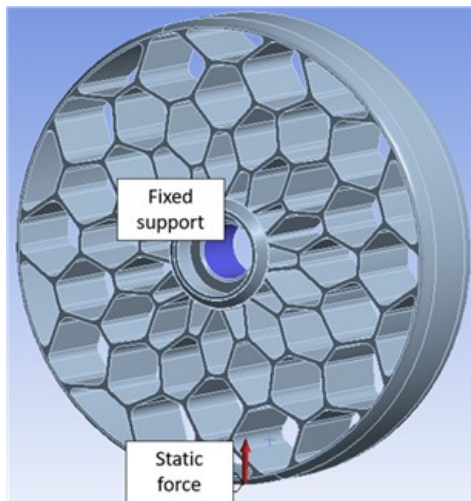


Figure 13. Finite elements model of the airless wheel.

(Figure 10) of the thermoelastic signal. As well known, the first one shows differential temperatures  $\Delta T$  that are linked to the sum of the principal components of the stress tensor. Also in this case, as already highlighted for the strain measurements, the loading apparatus used for transferring the load to the airless wheel hub plays a key role in determining the effective stress level to which the structure is subjected to. However, for both the PPR and the PLA samples, TSA guarantees the correct identification of the most stressed regions, which are found to be located at the vertex connections of the beams and to be confined to the lower sectors of the wheel. TSA measurements were performed out of the frontal view of the wheel, i.e. by tilting the optical axis of the IR camera with respect to the wheel axis. More in detail, camera-wheel relative angles of  $35^\circ$  and  $45^\circ$  were used for the PPR and PLA samples respectively. This configuration was introduced because the frontal view was subject to large edge effects due to the thin shaped beams.

Specifically, for the PPR sample, the rhombic and mixed configurations (Figure 9 a and Figure 9 b) exhibit a wide load distribution, marked at the vertex connections of the beams and at the sectors crossed by the loading line. Contrarily, in the trapezoidal configuration (Figure 9 c) the most stressed areas are reduced and concentrated in the lower sectors of the wheel. Comparing the trapezoidal configurations of the PPR with that of the PLA, the latter (Figure 9 d) presents a more limited load amplitude. Phase distribution (Figure 10) is in line with the expected distributions for all the wheel-test configurations.

### 3.3. CP mapping

The wheel-ground contact influences both the motion transfer and the wear of the rubber tread. Therefore, the evaluation of the CPs is useful for estimating both the functionality and stability of a vehicle.

As an example, Figure 11 shows the increment of the CPs for the trapezoidal configuration of the PPR wheel. The CP maps show quite a good symmetry: the small dissimilarities are due to the connection of the airless wheel to the loading apparatus and the relative geometric tolerances. It is evident that the lattice structure has a decisive influence on the redistribution of the load. Indeed, the beams, as previously emphasized, are the most rigid part of the airless wheel, hence the greatest CPs are estimated in correspondence with their mark on the ground. This well matches the results obtained on the strain analysis when the wheel is tested in the same topology arrangement (Figure 7 c).

Figure 12 compares the CP maps of the three different configurations at the maximum load (i.e. 200 N) on the PPR wheel. Also in this case, it is possible to identify a good symmetry, except for the mixed configuration. The largest contact area is that of the trapezoidal configuration, while the average CP is greater for the mixed one. Finally, the rhombic configuration shows the smallest contact area, but also the best symmetry. The maximum value of the CP is highlighted in correspondence with the beam of the mixed configuration. In both cases, mixed and rhombic configuration, the buckling effect would seem to be negligible due to the short arc of the external ring of the wheel between two successive beams.

### 3.4. Finite elements analysis

As a further analysis, a finite elements model (Figure 13) of the airless wheel was developed. This model was created to calculate the displacements and the strains of the wheel in ideal conditions (in terms of both geometries, loads and constraints).

The structure was meshed with about 2.5 million of solid tetrahedral elements, considering a fixed support at the wheel hub and a vertical static force at the wheel-ground interface. Furthermore, to improve the computation resolution, the mesh quality was refined on those areas where stress and strain are expected to be more relevant (Figure 14).

As an example, Figure 15 displays the maps relative to the computation of the Y-displacement and the Y-strain, for the PLA airless wheel printed in FDM. The numerical simulation highlights the same trends observed in the experimental results. The computed strain closely resembles the real one, showing that the interconnection segments of the lattice structure are mainly subjected to bending, exhibiting both tensile and compression stresses. Hence, the presented model might be used to analyze alternative configurations of the lattice geometry, laying the foundations for a structural optimization of the topology of the whole airless wheel.

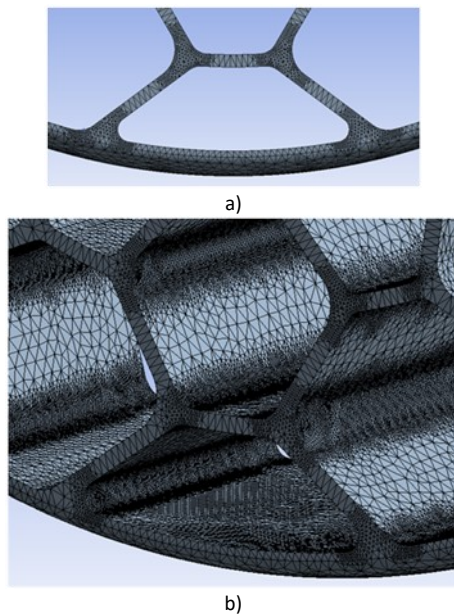


Figure 14. Details of the mesh quality of the airless wheel in a) frontal view and in b) 45° view.

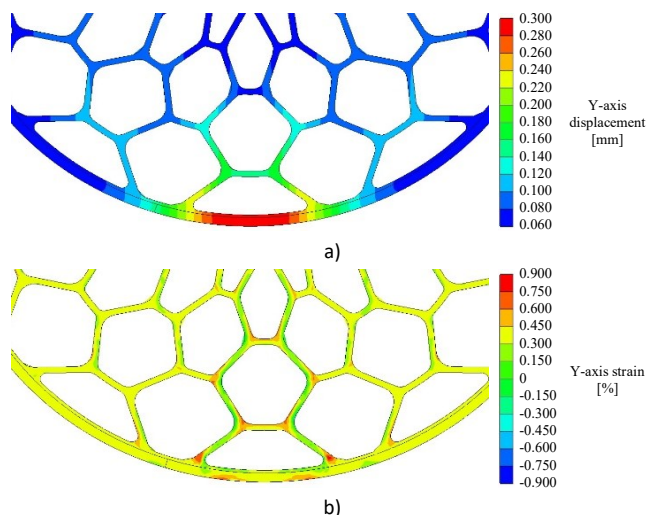


Figure 15. Finite element analysis of the airless wheel: a) Y-displacement and b) Y-strain at a load of 250 N on the PLA sample.

#### 4. CONCLUSIONS

This paper addresses the applicability of non-contact techniques, such as DIC and TSA, to measure the actual stress-strain field of complex lattice structures printed in AM. The chosen structure is based on the innovative airless wheel concept. This type of design could be widely applied for different vehicle models, taking advantage of its specific features. Globally, a puncture-proof wheel improves safety and reliability by reducing its replacement due to critical events and preventing the rapid decrease in vehicle stability. Furthermore, the mechanical response of a such structure could be enhanced by increasing the adhesion to the road surface and limiting the tread wear. Specifically, the use of an airless wheel could be heterogeneous. For example, it could be a good solution for skateboards, exploiting the high deformability of the lattice structure, or for aircrafts and aerospace vehicles thanks to the possibility of reducing weight maintaining the same performance. In summary,

the airless wheel should be of great interest to the next generation of full-electric cars.

An airless wheel prototype, manufactured by different 3D printing technologies (FDM and SLA) and made with different polymeric materials (PLA and PPR) has been tested by employing DIC and TSA techniques. The wheel-ground interaction has been studied by mapping the CPs. A parametric finite elements model of the same wheel has been developed. Furthermore, the experimental tests have been performed in two separated laboratories also using specific loading systems and instrumentation.

The results achieved have demonstrated some critical aspects that should be considered in the characterization of such a system: the type of material used for manufacturing the sample, the loading system and the topology of the lattice structure. In this sense, considering a numerical model previously validated at least in terms of contact pressure distribution, can help in dealing with these issues. Indeed, the proposed model might be used to analyze alternative configurations of the lattice geometry, laying the foundations for a structural optimization of the lattice topology with specific objective functions (e.g., uniform stress distribution or minimum weight). According to these outcomes, the present study has then confirmed the effectiveness of the non-contact techniques (DIC and TSA) for measuring the spatial distribution of both strain and stress fields in functional and complex structures obtained from AM. Specifically, these investigation techniques have shown that the mechanical response of a lattice structure exhibits considerable complexity. In fact, although strain and stress are well distributed over almost all regions, concentrations have been identified in correspondence of the nodes of the trabeculae and in the lower sectors of the wheel. For example, this suggests moving towards a topological optimization that involves increasing the thickness of the trabeculae at the nodes and along the external ring, thinning the section of the trabeculae at their centerline and reducing the excess of material closer to the wheel hub.

#### REFERENCES

- [1] T. D. Ngo, A. Kashani, G. Imbalzano, K. T. Nguyen, D. Hui, Additive manufacturing (3D printing): a review of materials, methods, applications and challenges, *Compos. B. Eng.* 143 (2018), pp. 172-196. DOI: [10.1016/j.compositesb.2018.02.012](https://doi.org/10.1016/j.compositesb.2018.02.012)
- [2] G. Luchao, W. Wenwang, S. Lijuan, F. Daining, Damage characterizations and simulation of selective laser melting fabricated 3D re-entrant lattices based on in-situ CT testing and geometric reconstruction, *Int. J. Mech. Sci.* 157-158 (2019), pp. 231-242. DOI: [10.1016/j.ijmecsci.2019.04.054](https://doi.org/10.1016/j.ijmecsci.2019.04.054)
- [3] T. Pereira, J.V. Kennedy, J. Potgieter, A comparison of traditional manufacturing vs additive manufacturing, the best method for the job, *Procedia. Manuf.* 30 (2019), pp. 11-18. DOI: [10.1016/j.promfg.2019.02.003](https://doi.org/10.1016/j.promfg.2019.02.003)
- [4] V. Asnani, D. Delap, C. Creager, The development of wheels for the Lunar Roving Vehicle, *J. Terramechanics* 46 (2009), pp. 89-103. DOI: [10.1016/j.jterra.2009.02.005](https://doi.org/10.1016/j.jterra.2009.02.005)
- [5] M. Siebold, Additive manufacturing for serial production of high-performance metal parts, *Mech. Eng.* 141 (2019), pp. 49-50. DOI: [10.1115/1.2019-MAY5](https://doi.org/10.1115/1.2019-MAY5)
- [6] F. Caiazzo, V. Alfieri, B.D. Bujazha, Additive manufacturing of biomorphic scaffolds for bone tissue engineering, *Int. J. Adv. Manuf. Syst.* 113 (2021), pp. 2909-2923. DOI: [10.1115/1.2019-MAY5](https://doi.org/10.1115/1.2019-MAY5)

- [7] E. Umaras, M.S. Tsuzuki, Additive manufacturing-considerations on geometric accuracy and factors of influence, *IFAC-PapersOnLine* 50, (2017), pp. 14940-14945.  
DOI: [10.1016/j.ifacol.2017.08.2545](https://doi.org/10.1016/j.ifacol.2017.08.2545)
- [8] A. Sutradhar, J. Park, D. Carrau, M.J. Miller, Experimental validation of 3D printed patient-specific implants using digital image correlation and finite element analysis, *Comput. Biol. Med.* 52 (2014), pp. 8-17.  
DOI: [10.1016/j.compbiomed.2014.06.002](https://doi.org/10.1016/j.compbiomed.2014.06.002)
- [9] L.S. Dimas, M.J. Buehler, Modeling and additive manufacturing of bio-inspired composites with tunable fracture mechanical properties, *Soft. Matter*. 10 (2014), pp. 4436-4442.  
DOI: [10.1039/C3SM52890A](https://doi.org/10.1039/C3SM52890A)
- [10] I. Gibson, D. Rosen, B. Stucker, M. Khorasani, Design for additive manufacturing, *Addit. Manuf. Tech.* (2021), pp. 555-607.  
DOI: [10.1007/978-3-030-56127-7\\_19](https://doi.org/10.1007/978-3-030-56127-7_19)
- [11] G. Liu, X. Zhang, X. Chen, Y. He, L. Cheng, M. Huo M, et al., Additive manufacturing of structural materials, *Mater. Sci. Eng. Rep.* 145 (2021), 100596.  
DOI: [10.1016/j.mserr.2020.100596](https://doi.org/10.1016/j.mserr.2020.100596)
- [12] A. Visco, C. Scolaro, T. Terracciano, R. Montanini, A. Quattrocchi, L. Torrisi, N. Restuccia, Static and dynamic characterization of biomedical polyethylene laser welding using biocompatible nano-particles, *EPJ Web of Conferences* 167 (2018), 05009.  
DOI: [10.1051/epiconf/201816705009](https://doi.org/10.1051/epiconf/201816705009)
- [13] V.M.R. Santos, A. Thompson, D. Sims-Waterhouse, I. Maskery, P. Woolliams, R. Leach, Design and characterisation of an additive manufacturing benchmarking artefact following a design-for-metrology approach, *Addit. Manuf.* 32 (2020), 100964.  
DOI: [10.1016/j.addma.2019.100964](https://doi.org/10.1016/j.addma.2019.100964)
- [14] C. Camposeco-Negrete, J. Varela-Soriano, J.J. Rojas-Carreón, The effects of printing parameters on quality, strength, mass, and processing time of polylactic acid specimens produced by additive manufacturing, *Prog. Addit. Manuf.* (2021), pp. 1-20.  
DOI: [10.1007/s40964-021-00198-y](https://doi.org/10.1007/s40964-021-00198-y)
- [15] N. Narra, J. Valášek, M. Hannula, P. Marcián, G.K. Sándor, J. Hyttinen, J. Wolff, Finite element analysis of customized reconstruction plates for mandibular continuity defect therapy, *J. Biomech.* 47 (2014), pp. 264-268.  
DOI: [10.1007/s40964-021-00198-y](https://doi.org/10.1007/s40964-021-00198-y)
- [16] C. Ling, A. Cernicchi, M.D. Gilchrist, P. Cardiff, Mechanical behaviour of additively-manufactured polymeric octet-truss lattice structures under quasi-static and dynamic compressive loading, *Mater. Des.* 162 (2019), pp. 106-118.  
DOI: [10.1016/j.matdes.2018.11.035](https://doi.org/10.1016/j.matdes.2018.11.035)
- [17] E. Alabort, D. Barba, R.C. Reed, Design of metallic bone by additive manufacturing, *Scr. Mater.* 164 (2019), pp. 110-114.  
DOI: [10.1016/j.scriptamat.2019.01.022](https://doi.org/10.1016/j.scriptamat.2019.01.022)
- [18] F. Li, J. Li, G. Xu, G. Liu, H. Kou, L. Zhou, Fabrication, pore structure and compressive behavior of anisotropic porous titanium for human trabecular bone implant applications, *J. Mech. Behav. Biomed. Mater.* 46 (2015), pp. 104-114.  
DOI: [10.1016/j.jmbbm.2015.02.023](https://doi.org/10.1016/j.jmbbm.2015.02.023)
- [19] G. Bi, C.N. Sun, H.C. Chen, F.L. Ng, C.C.K. Ma, Microstructure and tensile properties of superalloy IN100 fabricated by micro-laser aided additive manufacturing. *Mater. Des.* 60 (2014), pp. 401-408.  
DOI: [10.1016/j.matdes.2014.04.020](https://doi.org/10.1016/j.matdes.2014.04.020)
- [20] F. Brenne, T. Niendorf, H.J. Maier, Additively manufactured cellular structures: Impact of microstructure and local strains on the monotonic and cyclic behavior under uniaxial and bending load, *J. Mater. Process. Technol.* 213 (2013), pp. 1558-1564.  
DOI: [10.1016/j.jmatprotec.2013.03.013](https://doi.org/10.1016/j.jmatprotec.2013.03.013)
- [21] B. Pan, K. Qian, H. Xie, A. Asundi, Two-dimensional digital image correlation for in-plane displacement and strain measurement: a review, *MST* 20 (2009), 062001.  
DOI: [10.1088/0957-0233/20/6/062001](https://doi.org/10.1088/0957-0233/20/6/062001)
- [22] F. Lo Savio, M. Bonfanti, G.M. Grasso, D. Alizzio, An experimental apparatus to evaluate the non-linearity of the acoustoelastic effect in rubber-like materials, *Polym. Test.* 80 (2019), 106133.  
DOI: [10.1016/j.polymertesting.2019.106133](https://doi.org/10.1016/j.polymertesting.2019.106133)
- [23] D. De Domenico, A. Quattrocchi, D. Alizzio, R. Montanini, S. Urso, G. Ricciardi, A. Recupero, Experimental characterization of the FRCM-concrete interface bond behavior assisted by digital image correlation, *Sensors* 21 (2021), 1154.  
DOI: [10.3390/s21041154](https://doi.org/10.3390/s21041154)
- [24] D. De Domenico, A. Quattrocchi, S. Urso, D. Alizzio, R. Montanini, G. Ricciardi, A. Recupero, Experimental Investigation on the Bond Behavior of FRCM-Concrete Interface via Digital Image Correlation, *Proc. of European Workshop on Structural Health Monitoring, July 2020* pp. 493-502.  
DOI: [10.1007/978-3-030-64908-1\\_46](https://doi.org/10.1007/978-3-030-64908-1_46)
- [25] N. Vanderesse, A. Richter, N. Nuño, P. Bocher, Measurement of deformation heterogeneities in additive manufactured lattice materials by Digital Image Correlation: Strain maps analysis and reliability assessment, *J. Mech. Behav. Biomed. Mater.* 86 (2018), pp. 397-408.  
DOI: [10.1016/j.jmbbm.2018.07.010](https://doi.org/10.1016/j.jmbbm.2018.07.010)
- [26] G. Allevi, M. Cibeca, R. Fioretti, R. Marsili, R. Montanini, G. Rossi, Qualification of additively manufactured aerospace brackets: A comparison between thermoelastic stress analysis and theoretical results, *Measurement* 126 (2018), pp. 252-258.  
DOI: [10.1016/j.measurement.2018.05.068](https://doi.org/10.1016/j.measurement.2018.05.068)
- [27] L. Capponi, J. Slavič, G. Rossi, M. Boltežar, Thermoelasticity-based modal damage identification, *Int. J. Fatigue* 137 (2020), 105661.  
DOI: [10.1016/j.ijfatigue.2020.105661](https://doi.org/10.1016/j.ijfatigue.2020.105661)
- [28] D. Palumbo, U. Galietti, Data correction for thermoelastic stress analysis on titanium components, *Exp. Mech.* 56 (2016), pp. 451-462.  
DOI: [10.1007/s11340-015-0115-0](https://doi.org/10.1007/s11340-015-0115-0)
- [29] A. Quattrocchi, D. Palumbo, D. Alizzio, U. Galietti, R. Montanini, Thermoelastic stress analysis of titanium biomedical spinal cages printed in 3D, *Proc. of QIRT2020, Porto, Portugal, 10 July 2020*, pp. 1-7.  
DOI: [10.21611/qirt.2020.098](https://doi.org/10.21611/qirt.2020.098)
- [30] G. Allevi, P. Castellini, P. Chiariotti, F. Docchio, R. Marsili, R. Montanini, A. Quattrocchi, R. Rossetti, G. Rossi, G. Sansoni, E.P. Tomasini, Qualification of additive manufactured trabecular structures using a multi-instrumental approach. *Proc. I2MTC 2019, Auckland, New Zealand, 20-23 May 2019*, pp. 1-6.  
DOI: [10.1109/I2MTC.2019.8826969](https://doi.org/10.1109/I2MTC.2019.8826969)
- [31] G. Allevi, L. Capponi, P. Castellini, P. Chiariotti, F. Docchio, F. Freni, R. Marsili, M. Nartarelli, R. Montanini, S. Pasinetti, A. Quattrocchi, R. Rossetti, G. Rossi, S. Sansoni, E.P. Tomasini, Investigating additive manufactured lattice structures: a multi-instrument approach, *IEEE TIM* 69 (2020), pp. 2459-2467.  
DOI: [10.1109/TIM.2019.2959293](https://doi.org/10.1109/TIM.2019.2959293)
- [32] R. Montanini, G. Rossi, A. Quattrocchi, D. Alizzio, L. Capponi, R. Marsili, A. Di Giacomo, T. Tocci, Structural characterization of complex lattice parts by means of optical non-contact measurements, *Proc. of I2MTC 2020, Dubrovnik, Croatia, 25-28 May 2020*, pp. 1-6.  
DOI: [10.1109/I2MTC43012.2020.9128771](https://doi.org/10.1109/I2MTC43012.2020.9128771)
- [33] Bridgestone Airless Tires. Online [Accessed 28 July 2022] <https://www.bridgestonetire.com/tread-and-trend/tire-talk/airless-concept-tires>
- [34] Michelin, GM take the air out of tires for passenger vehicles. Online [Accessed 28 July 2022] <https://www.michelin.com/en/press-releases/michelin-gm-take-the-air-out-of-tires-for-passenger-vehicles/>
- [35] H. Wang, H. Xie, Y. Li, J. Zhu, Fabrication of micro-scale speckle pattern and its applications for deformation measurement, *MST*, 3'23 (2012), 035402.  
DOI: [10.1088/0957-0233/23/3/035402](https://doi.org/10.1088/0957-0233/23/3/035402)